Electrochimica Acta 562 (2026) 148509

Contents lists available at ScienceDirect

Electrochimica Acta

journal homepage: www.journals.elsevier.com/electrochimica-acta

Bubble resistance in near-zero-gap alkaline water electrolysis

W.L. van der Does [a,*], N. Valle [b], J.W. Haverkort [a]

[a] Delft University of Technology, Process & Energy Department, Leeghwaterstraat 39, Delft, 2628 CB Delft, The Netherlands
[b] Delft University of Technology, Ship Hydromechanics and Structures, Mekelweg 2, Delft, 2628 CD Delft, The Netherlands

ARTICLE INFO

Keywords:
Alkaline water electrolysis
Bubble layer resistance
Zero-gap
CFD
Electrochemical engineering

ABSTRACT

Modern alkaline water electrolysers for hydrogen production often use a zero-gap configuration in which electrodes are pressed directly against the separator. Counterintuitively, the inclusion of a small electrode-diaphragm gap was previously shown to reduce the cell potential significantly. This work aims to understand, quantify, and model this effect, and take first steps towards optimisation of the gap width. We present experimental measurements and simulations of the cell potential and kinetic and ohmic losses for expanded metal electrodes. We find that the configuration with our smallest used gap, created using a 60 μm spacer, yields the lowest cell potential, while the zero-gap configuration incurs additional voltage losses of approximately 80 mV at a current density of 10^4 A/m^2. This can be explained by bubbles and gas films in between the electrode and diaphragm, which block part of the diaphragm and electrode area. We introduce an analytical model that predicts the vertical gas fraction and current density distribution in the electrode-diaphragm gap, which is in good agreement with experimental and simulation results. For a maximum gas fraction below 0.7, the model can explain why there is no optimal gap width based solely on the gap resistance. Instead, the gap allows gas to escape, which mitigates the additional zero-gap overpotential. Our findings confirm, explain, and quantify that intentionally adding a small gap can be an effective way to improve the performance of alkaline electrolysers with perforated plate-like electrodes.

1. Introduction

Industrial electrochemical processes such as the chlor-alkali process, water electrolysis, and metal electrowinning use gas-evolving electrodes. These processes often employ a zero-gap configuration in which porous or plate electrodes with perforations are pressed directly against the diaphragm separating the cathodic and anodic compartments [1]. The zero-gap configuration is an improvement over the parallel-plate configuration, as it reduces the distance between the electrodes and directs the electrogenerated gases to the back side of the electrodes, thereby reducing the ohmic resistance [2]. This is expected to minimise ohmic losses, but in alkaline water electrolysis, zero-gap configurations often exhibit a significantly higher resistance than that of just the diaphragm [3]. Kienzlen et al. [4] showed that the reaction preferably takes place on the surface of the electrode facing the diaphragm, and concludes that a small gap in between the diaphragm and electrodes is essential. When the reaction occurs at the front face of the electrodes, the current distributes more evenly and the distance the ions travel between the electrodes is minimised. However, subsequent studies have shown that the higher resistance often found in zero-gap configurations can be explained by partial or full inactivation of the front face of the electrodes by gas films [3,5]. Previous works show that introducing a small gap between the diaphragm and electrode reduces these additional losses and significantly reduces the cell potential [4,6]. Furthermore, gas crossover across the diaphragm is a serious safety risk for alkaline water electrolysers [7] and the inclusion of a small electrode-diaphragm gap was shown to reduce crossover greatly [8].

In the traditional electrolyser design, several studies have investigated what should be the ideal distance between the electrodes, or between the electrode and diaphragm in the case of a divided cell, with varying outcomes. For an electrolyte with a constant resistivity, this ideal distance would be as small as possible. However, for gas-evolving electrolytes, the effective resistivity of the electrolyte will be increased by the gas bubbles. Early models predicting the conductivity of the inter-electrode gap [9] did not include a maximum gas fraction, so as the gas fraction tends to one, the conductivity tends to zero, and no more gas is produced. This naturally limits the gas fraction to one. Ref. [10] finds experimentally an optimal gap of 1–2 mm, but only for current densities above 0.5 A/cm^2 and heights above 1 cm. Additionally, they find that a hydrophobic electrode treatment reduces the cell potential, with an optimal gap of 2 mm. Ref. [11] found that the increase in gap conductivity and increase in gap width were balanced

* Corresponding author.
E-mail address: W.L.vanderDoes@tudelft.nl (W.L. van der Does).

https://doi.org/10.1016/j.electacta.2026.148509
Received 23 December 2025; Received in revised form 10 February 2026; Accepted 20 February 2026
Available online 27 February 2026

Nomenclature

$\hat{\mathbf{n}}$	Normal vector
$\hat{\mathbf{t}}$	Tangential unit vector
$\hat{\mathbf{z}}$	Unit vector in the z-direction
$\mathbf{i}$	Electrolyte current density [A/m^2]
$\mathbf{K}$	Stress tensor [Pa]
$\mathbf{U}$	Volume-averaged mixture velocity [m/s]
$\mathbf{u}$	Velocity [m/s]
$\mathbf{u}_{\mathrm{Hd}}$	Hydrodynamic diffusion slip velocity [m/s]
$\mathbf{u}_{\mathrm{Sd}}$	Shear diffusion slip velocity [m/s]
$\mathbf{u}_{\mathrm{Sp}}$	Solid pressure slip velocity [m/s]
$\mathbf{u}_{\mathrm{St}}$	Stokes slip velocity [m/s]
$\mathbf{U}_{\mathrm{s}}$	Slip flux or drift flux [m/s]
$\mathbf{u}_{\mathrm{s}}$	Slip velocity [m/s]
$\mathbf{U}_{\mathrm{m}}$	Mass-averaged mixture velocity [m/s]
$\mathcal{V}_{\mathrm{m}}$	Molar volume [m^3/mol]
A_{e}	Electrode surface area [m^2]
A_{geo}	Geometrical/diaphragm surface area [m^2]
b	Tafel slope [V]
D	Hydrodynamic diffusivity [m^2/s]
d_{b}	Bubble diameter [m]
E	Potential [V]
f	Bubble swarm hindrance function
H	Electrode height [m]
j	Current density [A/m^2]
j_*	Exchange current density [A/m^2]
$j_\perp$	Local current density on electrode surface [A/m^2]
l_{b}	Characteristic length $\left(12\mu U_{\mathrm{g}} z/\rho g \varepsilon_{\mathrm{m}}\right)^{1/3}$ [m]
n	Electrons per molecule electrogenerated gas
p	Pressure [Pa]
p_{s}	Solid pressure [Pa]
R_{dia}	Diaphragm resistance [Ω m^2]
R_{tr}	Transport resistance around electrodes [Ω m^2]
R_{zg}	Zero-gap additional resistance [Ω m^2]
T	Temperature
U_{g}	Volumetric gas flux at the electrode [m/s]
W	Vertical velocity component [m/s]
$W_{\mathrm{g,gap}}$	Vertical gas velocity in electrode-diaphragm gap [m/s]
w_{St}	Bubble rise velocity [m/s]
x	Horizontal coordinate [m]
z	Vertical coordinate [m]
z_{c}	Characteristic height for plume development [m]

Constants

F	Faraday's constant 96485 [C/mol]
g	Gravitational acceleration 9.81 [m/s^2]
R	Gas constant 8.314 [J/mol/K]

Greek variables

α	Charge transfer coefficient
η	Activation overpotential [V]
$\gamma_{0/1/2}$	Solid pressure model parameters
κ	Effective electrolyte conductivity [S/m]
κ_0	Electrolyte conductivity [S/m]
μ	Dynamic viscosity [Pa/s]
Φ	Electrode potential [V]
ϕ	Electrolyte potential [V]
ρ	Density [kg/m^3]
ε	Void fraction
$\varepsilon_{\mathrm{max}}$	Maximum gas fraction solid pressure model
$\varepsilon_{\mathrm{min}}$	Minimum gas fraction solid pressure model
ε_{m}	Maximum gas fraction analytical model
ζ	Electrode-diaphragm blockage by bubbles

Subscripts

∞	Condition at infinite height
a	Anode
cell	Cell
c	Cathode
eff	Effective/equivalent
eq	Equilibrium conditions
g	Gas phase
in	Inlet
l	Liquid phase
m	Mixture
opt	Optimal
out	Outlet

to such a degree that the ohmic drop often hardly varied with gap width in the tested range between 2 and 7 mm.

The maximum gas fraction occurring in alkaline water electrolysis may, in reality, be well below one. Strong electrolytes inhibit coalescence, and spherical bubbles of similar size cannot fill the entire space. Empirically, maximum gas fractions as low as 0.2 have been claimed [12,13]. For tall electrolysers, a larger value of 0.69 was reported [14] and a transition to slug flow can be observed [14,15].

A maximum gas fraction can be included in vertical gas distribution models to more closely match physical conditions in electolysers [12, 16], and in this case, the optimal gap distance becomes zero [17] for a constant liquid flow rate. However, in the case of a natural convective flow, a decreasing gap width also decreases the liquid flow rate, and a finite gap can be beneficial [18]. For typical values, Ref. [19] finds the gap width that minimises the ohmic drop to be in the millimetre range. However, all these works consider traditional parallel-plate electrolyser configurations in which all the gas that is produced remains in the gap. Perforated electrodes allow most of the gas to be diverted to the back side, and a much smaller inter-electrode distance will be preferable.

Very little work has been done to study the optimal electrode gap width with perforated electrodes. The experimental study in Ref. [20] used 89 cm-tall stainless steel electrodes in various flow configurations and with open electrode areas in the range 0%–60% perforation. For flat-plate electrodes, they find an optimal gap distance for forced, blocked, and natural convection, whereas for plates with more than 10% open area, the smallest tested gap width of 3 mm performs best. For 10–15 cm tall electrodes [21] it was found that the ohmic drop was lowest for a 1 cm gap with flattened expanded metal electrodes. For unflattened electrodes, no such optimum was found and the smaller the gap, the lower the ohmic drop. We note that the smallest tested value was a rather large 3 mm. For larger 0.5 m tall electrodes, Ref. [22] found for expanded metals that a gap between 1–3 mm only increased the cell voltage over a zero gap. It was concluded that for these still relatively large gaps, as also supposed in the model of Ref. [23], the gas was primarily concentrated in a plume thinner than the gap.

The gas fraction and resistivity between the electrodes in a vertical electrolyser evolve with height, as the gas is produced at the electrode surfaces. This results in an inhomogeneous vertical distribution of the current density in the electrolyser [20,24–26]. Consequently, the optimal gap width likely depends on the total height of the electrodes. While no studies have explicitly investigated the optimal gap width for different electrolyser heights, several works have attempted to model the vertical gas fraction and current distribution [9,27–32]. However, these works again consider electrolyser configurations in which all the gas that is produced remains in the gap.

Lab experiments have shown a significant improvement over zero-gap using a 0.2 mm gap when using expanded metal electrodes [6] as was claimed to be optimal in a patent [33]. However, recent X-ray experiments [34] found a zero gap to outperform configurations with a 0.1–0.3 mm gap, which is in contrast with previous literature findings [4,6]. The authors mention as a possible explanation a lower compression of the electrodes and diaphragm due to the construction of the cell. It has often been speculated that zero-gap is not always achieved in experiments [35]. Aside from the influence of the construction of the cell, some experimental work even indicates that the exact gap distance can change significantly and suddenly during an experiment [8], as gas slugs build up over seconds [6,36,37]. Therefore, significant variability in these results is expected.

Several models exist that simulate current distribution effects with resolved electrodes in a small-gap configuration [3,38], but these approaches all assume a fixed gap gas fraction. Recently, we found [39] that a maximum gas fraction can be incorporated into a mixture model to describe bubble dispersion and predict experimental bubble overpotentials, using a solid-pressure term. This approach allows a computational approach to predict the intertwined overpotential due to bubble-induced resistance and electrochemical activation losses with two-dimensional resolved electrodes.

A small gap between the electrodes and diaphragm has the potential to significantly reduce cell potential and reduce gas cross-over; however, the understanding of the underlying mechanisms is currently still lacking. In this study, we employ a combined experimental and theoretical approach, using experiments with varying electrode-diaphragm gap width, CFD, and an analytical hydrodynamic model to investigate the optimal gap width in a near-zero-gap water electrolyser.

The aim of this study is to improve the understanding of the voltage losses incurred in the zero-gap configuration for alkaline water electrolysis. Additionally, we investigate the effect of electrode-diaphragm gap width on the ohmic resistance and cell potential of an alkaline water electrolysis cell. We present an analytical model for the electrode-diaphragm gap resistance and vertical current distribution in near-zero-gap alkaline water electrolysis cell. This work quantifies the additional voltage losses in the zero-gap configuration and the bubble-induced ohmic losses in a small electrode-diaphragm gap, and presents a first step towards optimisation of the gap width.

The paper is organised as follows: Section 2 introduces the experimental set-up and approach used to test the different electrode-diaphragm gap widths. Section 3 presents the computational approach used to model the multiphase flow and electrochemistry, followed by Section 4, which proposes an analytical model to describe the development of the gas fraction within the electrode-diaphragm gap. The experimental and computational results are presented and compared to this analytical model in Section 5, which contains the interpretation and discussion of the results. At the end of this section, we present a theory for the optimal electrode-diaphragm gap width.

2. Experimental methods

2.1. Zero-gap cell design

This study employs RuO_2-coated nickel expanded metal electrodes supplied by Permascand AB, which feature eye-shaped holes of approximately 3×1 mm, electrode thickness of 0.5 mm, and an open area fraction of approximately 50%. The cathode, anode, and Zirfon Perl UTP 500 diaphragm were sandwiched in between two poly(methyl methacrylate) (PMMA) frames with a window cut-out of 15 cm^2 to achieve the zero-gap configuration shown in Fig. 1. Ten M5 nylon bolts threaded through the PMMA frame and fastened with nylon nuts hold the different parts in place. The PMMA frame has an inner cut-out of 6 by 2.5 cm which gives 15 cm^2 of exposed electrode area. The electrodes feature a L-shaped design where a narrow strip of electrode extends upwards as a terminal to connect to the potentiostat, as shown in Fig. 1. The electrodes are slightly larger than the cut-out in the PMMA frame which overlaps the electrodes by approximately 2 mm on each side. This effectively achieves a consistent electrode-diaphragm assembly. Nylon woven meshes supplied by Sefar Nitex with the same dimensions and window cut-out were used to achieve a consistent electrode-diaphragm gap width of 60–910 μm. These mesh frames are placed between the electrodes and diaphragm, and are applied symmetrically on both sides. All components of the electrochemical cell, as well as the assembled cell, are shown in Fig. 1.

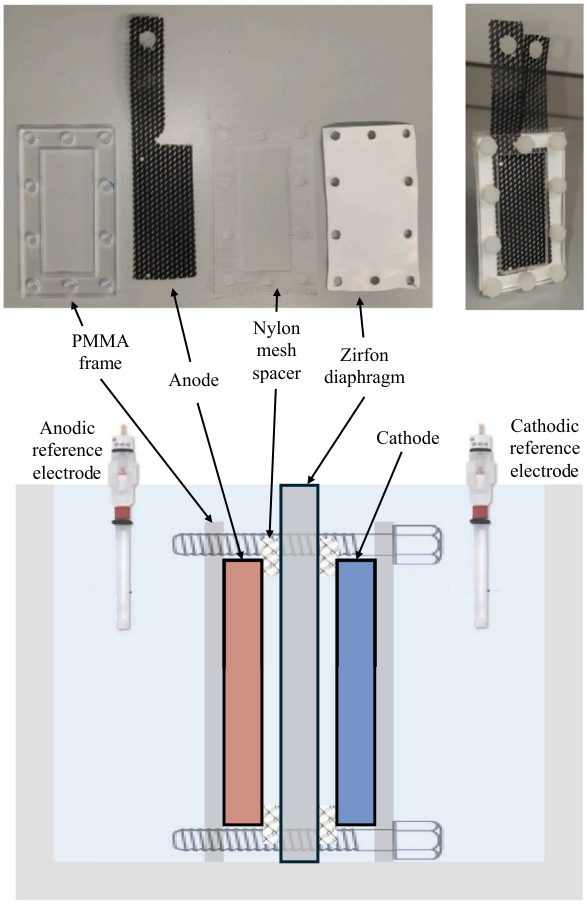

Fig. 1. Top left: Components of a half-cell in order of assembly. From left to right: PMMA frame, expanded metal RuO_2 electrode, Nylon mesh spacer, Zirfon diaphragm. The electrode overlaps with the nylon mesh spacer around the edges, which creates the electrode-diaphragm gap. The same thickness mesh spacer is used on the anodic and cathodic side for a symmetrical electrode-diaphragm gap. Top right: Assembled electrode-diaphragm assembly with mesh spacers. Bottom: schematic representation of the experimental set-up with the electrode-diaphragm assembly and two reference electrodes.

2.2. Experimental set-up

The experimental set-up described in [5] is used for this study. The zero-gap cell described in the previous section is submerged in a small

container filled with a 30 wt% potassium hydroxide (KOH) electrolyte solution made with Milli-Q water and 85% purity KOH pellets from Sigma Aldrich.

The voltage was measured using a Gamry Reference 3000 potentiostat with a 30 A booster. For each experiment, the electrodes were preconditioned at a constant current of 10^4 A/m^2 for 600 s. This was immediately followed with a current sweep from 10^4 A/m^2 down to 6.67 A/m^2 in 31 steps on a logarithmic scale, then back up to 10^4 A/m^2 in the same amount of steps and back down again to 6.67 A/m^2. Each current was maintained for 30 s, after which the current was interrupted for 1 s before initiating the next step. The voltage applied by the potentiostat quickly stabilised over the first half of the 30 s, thus for each measurement the cell potential over the last 5 s is used. The time-averaged voltages of the last 5 s of the up-sweep and second down-sweep were averaged again to give the reported voltage per current density. While the differences between the up-sweep and the first and second down-sweeps were found to be negligible, the experimental protocol duplicated from [5] excluded the results from the first down-sweep.

The experiments were conducted at a fixed electrolyte temperature of 80 °C. The electrolyte-filled container with the electrochemical cell is placed inside a stirred one-litre beaker of water which contained a copper coil. The container has stainless steel endplates to allow for better thermal management. A Lauda RC6-CP circulator was used to pump water through the copper coil. The temperature in the electrolyte was measured using a PT-100 temperature sensor, and this temperature measurement was used in a control loop by the Lauda circulator to regulate the temperature of the electrolyte. The maximum measured fluctuation of the electrolyte temperature was around ±1 °C.

Two EF-1369 Hg/HgO reference electrodes by BASi® filled with 1 M sodium hydroxide solution were placed in the anolyte and catholyte to measure relative potential between the reference electrodes and the anode and cathode, respectively. Additionally, the potential between the two reference electrodes gives a measurement of the ohmic drop across the zero-gap configuration. The reference electrode potential is converted to give a potential versus RHE [40]:

$$E_i = E_{Hg/HgO} + \frac{2.303RT}{F}\text{pH} + E^\circ_{Hg/HgO} - \frac{RT}{2F}\ln\frac{(\gamma_{OH^-}c_{OH^-})^2}{a_{H_2O}} \quad (1)$$

where $E_{Hg/HgO}$ is the measured reference electrode potential, and a pH of 14 is used for the KOH electrolyte solution [41]. The standard potential for the Hg/HgO reference electrode at a temperature of 80 °C $E^\circ_{Hg/HgO} = 0.026$ V [42] is corrected for the activity of hydroxide and water in the 1 M sodium hydroxide internal solution of the reference electrodes, with a hydroxide activity coefficient of $\gamma_{OH^-} = 0.61$ and water activity of $a_{H_2O} = 0.967$ [41]. The potential of the reference electrodes, along with the potential of the anode and the cathode, was recorded with a NI-6002 data acquisition unit and logged using NI LabView. The potential difference between the anode and cathode was also measured using the potentiostat to validate the NI-6002 measurements.

This study considers a natural convection case, different from the forced convection often used in industry. In bipolar stacks, the flow rate is often strongly limited by the necessarily narrow inlets and outlets required to reduce shunt currents, and flow rates are set to the minimum values to remove heat [43]. The contribution of forced flow on velocity is then of the order of millimetres per second, much smaller than the contribution of centimetres per second induced by buoyancy. Therefore, such a small forced flow contribution is expected to have little effect on our results.

3. Computational model

3.1. Multiphase flow

The simulations are based on the model presented in [39]. A two-dimensional geometry representing a cross-section of an expanded metal electrode is used, shown schematically in Fig. 2. The holes in the electrodes are 1 mm tall and are spaced with a pitch of 2 mm. This correlates to the short way of opening, the length of the short diamond diagonal, of 1 mm of the 3 × 1 mm holes in the electrode. The electrodes have a thickness of 0.5 mm, and have an open area of 50%. The domain height of 60 mm then contains a total of 30 holes in each electrode. The multiphase flow is described using the mixture model for laminar, incompressible flow [44,45]. For the small electrolytic bubbles, surface tension dominates and the bubbles are spherical. Additionally, due to the high KOH concentrations in the electrolyte, coalescence is strongly reduced, so that the simulations are simplified by taking a constant bubble diameter [46,47]. To reduce computational expense, the mixture model uses a volume-averaged gas fraction ε to represent the gas present in the mixture rather than resolving individual bubbles. The volume-averaged mixture velocity is then given by $\mathbf{U} = (1-\varepsilon)\mathbf{u}_l + \varepsilon\mathbf{u}_g$, where $\mathbf{u}_l$ and $\mathbf{u}_g$ are the liquid and gas velocities, respectively. The gas density is negligible compared to the liquid density ρ_l so the mixture density ρ_m can be represented as $\rho_m = (1-\varepsilon)\rho_l$. The mass-averaged mixture velocity $\mathbf{U}_m$ is then given by $\rho_m\mathbf{U}_m = \rho_l(1-\varepsilon)\mathbf{u}_l + \rho_g\varepsilon\mathbf{u}_g$. The continuity equation for the mixture in steady state is given by

$$\nabla\cdot\mathbf{U}_m = 0 \quad (2)$$

The mixture model solves a single momentum equation that represents the transport of the mixture as a whole, rather than solving for

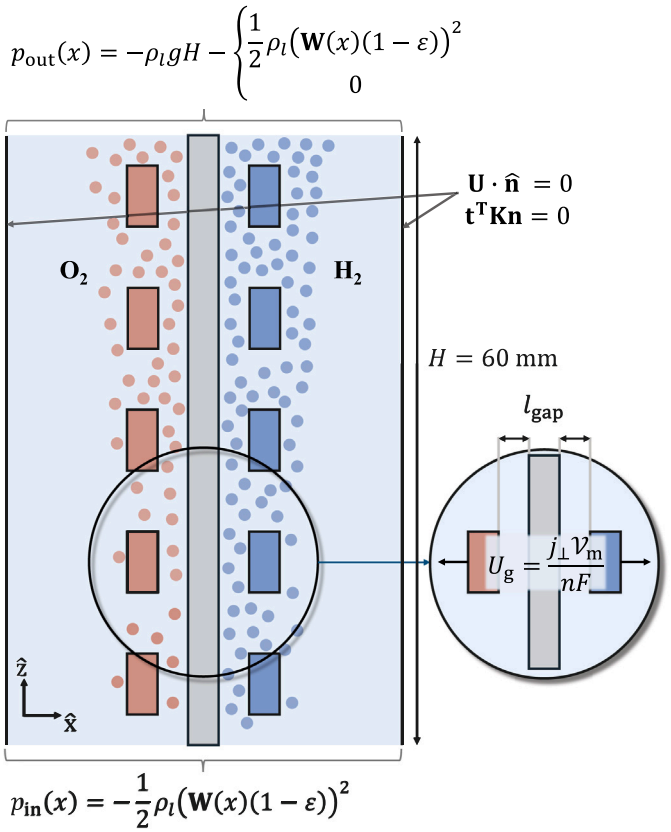

Fig. 2. Representation of the two-dimensional simulation domain, coordinate system, and boundary conditions. The boundary conditions are discussed in further detail in Sections 3.1 and 3.2. Red and blue rectangles are anode and cathode segments, respectively. These segments represent the cross-sectional area of an expanded metal electrode. Five electrode segments are shown on each side in the schematic, but the 60 mm tall simulation geometry contains 30 pairs of electrode segments. The grey rectangle in between the electrodes represents the diaphragm and the gap between the electrodes and the diaphragm is indicated by l_{gap}.

the transport of liquid and gas separately. With negligible gas density, the momentum equation for the mixture in steady state is given by

$$\rho_m \mathbf{U}_m \cdot \nabla \mathbf{U}_m = -\nabla p + \nabla \cdot \mathbf{K} - \rho_m g \hat{\mathbf{z}} \tag{3}$$

where $\mathbf{K}$ represents the mixture viscous stress tensor, and the mixture viscosity μ_m is given by $\mu_m = \frac{\mu_l}{1-\varepsilon}$ [48,49]. The mixture model uses Eqs. (2) and (3) to describe the transport of the volume-averaged mixture. The relative motion between the liquid and gas phases is given by the slip velocity:

$$\mathbf{u}_s = \mathbf{u}_g - \mathbf{u}_l \tag{4}$$

The volume of gas is conserved and the model does not include mass transport between the gas and liquid, hence $\nabla \cdot (\varepsilon \mathbf{u}_g) = 0$ and the gas continuity equation is given by

$$\mathbf{U} \cdot \nabla \varepsilon + \nabla \cdot \mathbf{U}_s = 0 \tag{5}$$

Where $\mathbf{U}_s = \varepsilon(1-\varepsilon)\mathbf{u}_s$ is the slip flux or drift flux. The difference in velocity between the gas and liquid phases is described by a combination of different sub-grid models, each representing a different slip mechanism:

$$\mathbf{u}_s = \mathbf{u}_{St} + \mathbf{u}_{Hd} + \mathbf{u}_{Sd} + \mathbf{u}_{Sp} \tag{6}$$

Where $\mathbf{u}_{St}$ represents Stokes' rise velocity, $\mathbf{u}_{Hd}$ represents slip due to hydrodynamic dispersion, $\mathbf{u}_{Sd}$ represents slip due to shear-induced diffusion, and $\mathbf{u}_{Sp}$ represents slip due to solid pressure.

In the mixture model, the slip velocities result from the assumption that all forces acting on the bubble are in equilibrium with the drag force, and no acceleration of the bubbles relative to the surrounding liquid occurs. The drag force is assumed to be described by Stokes' drag, which gives the following slip velocity models:

$$\mathbf{u}_{St} = f(\varepsilon) w_{St} \hat{\mathbf{z}} \tag{7}$$

$$\mathbf{u}_{Hd} = -f(\varepsilon) \frac{d_b w_{St}}{2} \frac{\nabla \varepsilon}{\varepsilon} \tag{8}$$

$$\mathbf{u}_{Sd} = -\frac{d_b^2}{4} \left| \frac{\partial w}{\partial x} + \frac{\partial u}{\partial z} \right| \frac{\varepsilon(1 + 0.5e^{8.8\varepsilon})}{3(1-\varepsilon)} \nabla \varepsilon \tag{9}$$

$$\mathbf{u}_{Sp} = \frac{d_b^2 \nabla p_s}{18 \mu \varepsilon} \tag{10}$$

where $w_{St} = \frac{\rho_l g d_b^2}{18 \mu_l}$ gives the terminal rise velocity of a single bubble with diameter d_b, and $f = (1-\varepsilon)^4$ is a hindrance function that represents hindrance in a swarm of rising bubbles. The local solid pressure is given by $\nabla p_s = \gamma_0 \rho_m g d_b \nabla \frac{(\varepsilon - \varepsilon_{min})^{\gamma_1}}{(\varepsilon_{max} - \varepsilon)^{\gamma_2}}$ [50]. The original formulation of the slip velocity models in Eq. (7)–(9) was developed for a bubbly flow along flat-plate electrodes [45], similar to the bulk flow region of the computational domain outside of the electrode-diaphragm assembly. In order to describe the bubble transport in confined regions such as the holes in the electrodes, and the electrode-diaphragm gap, the solid pressure model in Eq. (10) is added to the original formulation from Ref. [45]. For a more elaborate discussion of the slip velocity models and this solid pressure model, the reader is referred to our previous publication [39].

The parameters used in these models are listed in Table 1. In this study, an effective bubble diameter is used which represents the rate of bubble dispersion inside the computational domain. While this effective bubble diameter in some cases can be larger than the electrode-diaphragm gap, the bubble size in alkaline water electrolysis is known to be polydisperse. Therefore, even if the electrode-diaphragm gap is smaller than the effective bubble diameter, bubble dispersion may still occur inside the electrode-diaphragm gap with smaller bubbles.

Fig. 2 shows the boundary conditions for the multiphase flow model. At the bottom and top outlet, a pressure boundary condition is used

$$(-p\mathbf{I} + \mathbf{K}) \cdot \hat{\mathbf{n}} = -p_{in/out} \hat{\mathbf{n}} \tag{11}$$

The hydrostatic pressure difference is included at the outlet, with a mixed hydrostatic and local Bernoulli boundary condition at the inlet and a fixed prescribed pressure at the outlet

$$p_{in}(x) = -\frac{1}{2} \rho_l (W(x)(1-\varepsilon))^2 \tag{12a}$$

$$p_{out}(x) = -\rho_l g H + \begin{cases} -\frac{1}{2}\rho_l (W(x)(1-\varepsilon))^2 & W(x) < 0 \\ 0 & W(x) \geq 0 \end{cases} \tag{12b}$$

where $W(x)$ is the vertical component of the volume-averaged mixture velocity $\mathbf{U}$. The application of the mixed hydrostatic and local Bernoulli pressure boundary condition best reproduced the return flow intensity on the inlet and outlet boundaries, as observed in natural convection experiments [51–53]. The external gas fraction at the outlet is set to $\varepsilon_{out} = 0$ to prevent any potential back-flow from re-introducing gas into the domain. At the outer vertical boundaries, a symmetry boundary condition is applied which represents no flow across the boundary and zero tangential viscous stresses:

$$\mathbf{U} \cdot \hat{\mathbf{n}} = 0 \tag{13a}$$

$$\mathbf{t}^T \mathbf{K} \hat{\mathbf{n}} = 0 \tag{13b}$$

A no-slip boundary condition is used for the mixture at the diaphragm surface:

$$\mathbf{U} = 0 \tag{14}$$

and at the surfaces of the electrodes, the gas flux and mixture velocity are given by:

$$\varepsilon \mathbf{u}_g = \mathbf{U} = -U_g \hat{\mathbf{n}} \tag{15}$$

where the mixture effectively has a no-slip condition parallel to the surface, and is set equal to the electrochemical gas production rate U_g perpendicular to the electrode surface. Faraday's Law connects this gas production rate to the local current density:

$$U_g = \frac{\mathcal{V}_m}{nF} j_\perp \tag{16}$$

where $\mathcal{V}_m = \frac{RT}{p}$ is the molar volume of gas given by the ideal gas law and n the number of electrons per gas molecule, which is 2 for hydrogen and 4 for oxygen.

3.2. Electrochemistry

In alkaline water electrolysis, hydrogen and oxygen are evolved at the cathode and anode, respectively, with the following reaction equations:

$$\text{Cathode}: \quad 4\,H_2O + 4\,e^- \longrightarrow 4\,OH^- + 2\,H_2$$

$$\text{Anode}: \quad 4\,OH^- \longrightarrow 2\,H_2O + O_2 + 4\,e^-$$

The electrolyte consists of a concentrated solution of KOH in water. In the reaction, hydroxide ions are produced at the cathode and consumed at the anode, acting as charge carrier to close the electrical circuit. At the high electrolyte concentrations used in alkaline water electrolysis, the concentration of the electrolyte is approximately homogeneous and the transport of ions in the electrolyte can be describe by Ohm's law:

$$\mathbf{i} = -\kappa \nabla \phi \tag{17}$$

where $\mathbf{i}$ is the electrolyte current density, κ is the effective conductivity, and ϕ is the local potential in the electrolyte. The effective conductivity is reduced by the presence of bubbles, which can be described by Bruggeman's relation:

$$\kappa = \kappa_0 (1-\varepsilon)^{3/2} \tag{18}$$

where κ_0 is the intrinsic electrolyte conductivity. The conductivity of the diaphragm is given by $\kappa_d = \kappa_0 \frac{\epsilon}{\tau^2}$ with $\frac{\epsilon}{\tau^2} = 0.35$ the ratio of

Table 1
Parameters used for the computational and theoretical model. The exchange current densities, charge transfer coefficients, and open circuit potential were obtained from reference electrode data from the experiments in this study as discussed in Section 5.1.

Temperature	T	353.15 K
Liquid density [55]	ρ_l	1260 kg/m^3
Liquid viscosity [55]	μ_l	0.95 mPa s
Bubble diameter H_2	d_{b,H_2}	120 µm
Bubble diameter O_2	d_{b,O_2}	120 µm
Anode exchange current density	$j_{*,a}$	7.1 A/m^2
Cathode exchange current density	$j_{*,c}$	31 A/m^2
Anode charge transfer coefficient	α_a	1.72
Cathode charge transfer coefficient	α_c	1.76
Equilibrium potential	E_{eq}	1.38 V
Electrolyte conductivity	κ_0	139.4 S m^{-1}
Solid pressure parameters [50]	γ_0	0.002
	γ_1	2
	γ_2	5
	ϵ_{min}	0
	ϵ_{max}	0.65
Analytical model maximum ϵ	ϵ_m	0.5

porosity and tortuosity squared [17,54]. The Butler–Volmer equation for concentration-independent kinetics is used to describe the electrode kinetics:

$$j_{\perp,a} = j_{*,a}\left(e^{\frac{\alpha_a F\eta}{RT}} - e^{-\frac{(n-\alpha_a)F\eta}{RT}}\right) \tag{19a}$$

$$j_{\perp,c} = -j_{*,c}\left(e^{\frac{(n-\alpha_c)F\eta}{RT}} - e^{-\frac{\alpha_c F\eta}{RT}}\right) \tag{19b}$$

where $j_{\perp,i}$ is the local current density at the electrode interface, $j_{*,i}$ is the exchange current density, α_i is the charge transfer coefficient, with i = a indicating anodic and i = c indicating cathodic, and the activation overpotential $\eta = (E-\phi) - (E-\phi)_{eq}$, with the electrode potential E, and the subscript eq denoting electrode potential values at $j_\perp = 0$.

At the anode the electrode potential is set to 0 V

$$E_a = 0 \tag{20}$$

and at the cathode an average geometrical current density j is applied so that is equal to the average local current density $j_\perp$ on the electrode surface

The cathode potential E_c is adjusted so that the average local current density on the electrode surface $j_\perp$ is equal to the geometrical current density

$$\frac{1}{A_{geo}}\int_{A_e} j_\perp \, dA_e = j \tag{21}$$

where A_e is the electrode surface area and A_{geo} is the geometrical surface area which relate to each other as $A_{geo} = \frac{2}{3}A_e$. As the electrode surface area is higher than the geometrical surface area, the current density at the electrode surface $j_\perp$ will on average be lower than the geometrical current density j. Here, we consider a 1 m wide electrode in the third, not modelled dimension, for simplicity. The parameters used in the simulations are given in Table 1.

3.3. Numerical methods

The computational component of this work uses the stationary solver in COMSOL Multiphysics v6.2 with first-order discretisation. Square mesh elements with a size of 25 µm × 25 µm were chosen based on the grid convergence study described in our previous work [39]. Inside the electrode-diaphragm gap, a minimum of 8 mesh elements are present for all simulation geometries.

4. Analytical model

4.1. Vertical gas fraction distribution

Gas is generated at the electrodes and initially primarily ends up in the electrode-diaphragm gap. This gas reduces the local density, which gives a buoyant force resulting in up-flow of the gas–liquid mixture in the gap. The model presented in this section is based on similar works [17,18]. The buoyant force resulting from the gas is balanced against a frictional pressure gradient p_f':

$$p_f' = \rho_l g\langle\epsilon\rangle \tag{22}$$

where ρ is the electrolyte density, g the gravitational acceleration, and $\langle\epsilon\rangle$ the horizontally averaged gas fraction inside the gap. We use Hagen–Poiseuille to balance the frictional pressure gradient with the liquid velocity

$$p_f' \approx \frac{12\mu}{l_{gap}^2} W_l \tag{23}$$

where μ is the liquid viscosity, l_{gap} is the electrode-diaphragm gap width, and W_l is the vertical component of the superficial liquid velocity in the gap. The vertical velocity components of the liquid and gas phases inside the gap are given by $w_g = \frac{W_{g,gap}}{\langle\epsilon\rangle}$ and $w_l = \frac{W_l}{1-\langle\epsilon\rangle}$. Here $W_{g,gap}$ is the superficial gas velocity inside the gap. Assuming a dispersed bubbly flow with a homogeneous gas fraction $\langle\epsilon\rangle$, and neglecting slip, Eq. (4) gives an expression for the average gas fraction in the gap:

$$\langle\epsilon\rangle = \frac{W_{g,gap}}{W_l + W_{g,gap}} \tag{24}$$

Since we neglect slip, the ratio between liquid and gas superficial velocity is described as $W_{g,gap} = \frac{W_l\epsilon}{1-\epsilon}$. Initially, the gas bubbles primarily end up in the electrode-diaphragm gap. However, at high superficial gas flow rates the gap fills up with bubbles and subsequent gas production results in dispersion of the gas to the back side of the electrodes. To include this complex effect in the model, we impose a maximum gas fraction inside the gap of ϵ_m. With $\epsilon = \epsilon_m$ we find an expression for the maximum gas superficial velocity in the gap $W_{g,max} = \frac{W_l\epsilon_m}{1-\epsilon_m}$. At low superficial gas velocities, we expect most of the gas bubbles to be produced in the electrode-diaphragm gap. As the gas fraction in the gap increases, bubble interactions force more gas to the outside of the electrode-diaphragm assembly. At high superficial gas velocities, the gas fraction in the gap approaches ϵ_m and the superficial gas velocity approaches $W_{g,max}$. We model this as

$$W_{g,gap} = \frac{1}{\frac{1}{W_g} + \frac{1}{W_{g,gap,max}}} \tag{25}$$

with the superficial velocity in the gap based on total gas superficial velocity $W_g = \frac{j\mathcal{V}_m z}{nFl_{gap}}$ to include the expected asymptotic behaviour at low and high W_g. Here, we assume a constant current distribution. Substitution of $W_{g,max}$ and $W_{g,gap}$ in Eq. (24) gives

$$\langle\epsilon\rangle \approx \frac{W_g}{W_l + \frac{W_g}{\epsilon_m}} = \epsilon_m \frac{W_l}{W_{l,max}} \tag{26}$$

where the second equation was obtained by substituting Eq. (23) in Eq. (22). Here, $W_{l,max} = \epsilon_m \rho g l_{gap}^2/12\mu$ is the maximum liquid flux obtained at the maximum gas fraction.

4.2. Analytical solution

Eq. (26) together with Eq. (22) and (23) gives a quadratic equation for W_l that is solved by

$$W_\mathrm{l} = W_\mathrm{g}\frac{\sqrt{\frac{4\varepsilon_\mathrm{m}W_\mathrm{l,max}}{W_\mathrm{g}}+1}-1}{2\varepsilon_\mathrm{m}} \approx \begin{cases}\sqrt{\frac{W_\mathrm{g}W_\mathrm{l,max}}{\varepsilon_\mathrm{m}}} & \frac{4\varepsilon_\mathrm{m}W_\mathrm{l,max}}{W_\mathrm{g}} \gg 1 \\ W_\mathrm{l,max} & \frac{4\varepsilon_\mathrm{m}W_\mathrm{l,max}}{W_\mathrm{g}} \ll 1\end{cases} \tag{27}$$

The second approximation results from $\sqrt{1+\epsilon} \approx 1+\epsilon/2$ for $\epsilon \ll 1$. For small values of W_g, the liquid flux increases with the square root of W_g. For large values, a maximum is attained. From Eq. (26), multiplication with $\varepsilon_\mathrm{m}/W_\mathrm{l,max} = 12\mu/\rho g l_\mathrm{gap}^2$ gives the gas fraction. Assuming the effective conductivity depends on the gas fraction according to Bruggeman's relation $\kappa = \kappa_0(1-\langle\varepsilon\rangle)^{3/2}$, the ohmic potential drop over the gap reads

$$\frac{jl_\mathrm{gap}}{\kappa_0(1-\langle\varepsilon\rangle)^{3/2}} = \frac{jl_\mathrm{gap}}{\kappa_0\left(1-\frac{\sqrt{\frac{4\varepsilon_\mathrm{m}l_\mathrm{gap}^3}{l_\mathrm{b}^3}+1}-1}{2l_\mathrm{gap}^3/l_\mathrm{b}^3}\right)^{3/2}} \tag{28}$$

where we used the conservation of gas volume $U_\mathrm{g}z = W_\mathrm{g}l_\mathrm{gap} = \frac{\mathcal{V}_\mathrm{m}}{nF}j$ and introduced the characteristic buoyant length-scale $l_\mathrm{b}^3 \equiv 12\mu U_\mathrm{g}z/\rho g\varepsilon_\mathrm{m}$.

4.3. Optimal gap thickness

Eq. (28) can be minimised by setting the derivative with respect to l_gap to zero. This gives $l_\mathrm{opt} \approx l_\mathrm{b}$ if we assume $\varepsilon_\mathrm{m} \approx 0.7$, or

$$l_\mathrm{gap,opt} \approx 2.6\left(\frac{\mu U_\mathrm{g}z}{\rho g}\right)^{1/3} \tag{29}$$

The prefactor increases up to 3.9 for $\varepsilon_\mathrm{m} = 1$, in which case $l_\mathrm{opt} \approx 1.7l_\mathrm{b}$. The exact solution is $\frac{l_\mathrm{gap}^3}{l_\mathrm{b}^3} = \frac{169\varepsilon_\mathrm{m}^2-88\varepsilon_\mathrm{m}-4+(13\varepsilon_\mathrm{m}-2)\sqrt{169\varepsilon_\mathrm{m}^2-124\varepsilon_\mathrm{m}+4}}{32\varepsilon_\mathrm{m}}$. A similar expression as Eq. (29) was previously obtained in Ref. [19] and recently re-derived in Ref. [18] in the context of a natural recirculation-driven electrolyser.

Interestingly, only for $\varepsilon_\mathrm{m} = 1$ this is an absolute minimum: for all other values a new absolute minimum arises and the ohmic drop becomes zero for $l_\mathrm{gap} = 0$. Another interesting finding is that the local minimum around $l_\mathrm{opt} \approx l_\mathrm{b}$ disappears for $\varepsilon_\mathrm{m} \lesssim 0.7$, see Fig. 3. Refs. [18,19] considered a maximum gas fraction of one only and this finding was not noted there. It may be an important subtlety as the maximum gas fraction may well be below 0.7, in which case our model predicts that a zero gap will be optimal.

Clearly the present model is a strong simplification of reality, nonetheless it may be useful to compare to experimental results. The absolute minimum at $l_\mathrm{gap} = 0$ for maximum gas fractions under 1 likely does not exist, and as seen in literature such configurations often suffer from additional voltage losses [3,6]. Neglecting this absolute minimum, Eq. (29) predicts that for $\varepsilon_\mathrm{m} \gtrsim 0.7$ a larger gap may be beneficial for larger heights and current densities. However, in case the maximum gas fraction is smaller than 0.7 a smaller gap will result in a lower ohmic resistance.

4.4. Vertical current density distribution

In the above analytical model we assumed a constant current density. With increasing height, the average gas fraction increases, increasing the ohmic drop that will lead to a decrease in current density as a function of height. In Ref. [17] an analytical solution was derived for the current density as a function of height in case $\varepsilon_\mathrm{m} = 1$. Here, we will generalise this and find an approximate relation for different values. We assume that the cell voltage can be approximately linearised with respect to current density so

$$V_\mathrm{cell} = V_\mathrm{eq} - \left(\eta + \frac{2jl_\mathrm{gap}}{\kappa} + \frac{jl_\mathrm{eff}}{\kappa_\mathrm{m}}\right) \tag{30}$$

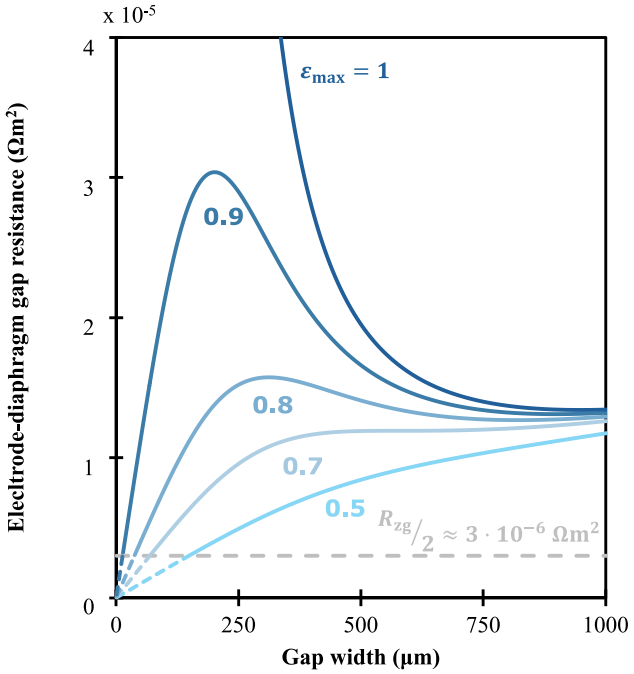

Fig. 3. Electrode-diaphragm gap resistance as predicted by Eq. (28) for a single gap (anode or cathode). For a maximum gas fraction of 1 in between the electrode and diaphragm, the model predicts an optimum gap width. Decreasing the maximum gas fraction to 0.9 gives a local minimum at similar gap width, with a global minimum for very small gaps. A maximum gas fraction of 0.7 gives a saddle point but no local minimum outside of the minimum for very small gaps. The grey dashed line indicates additional resistance due to a zero-gap induced overpotential R_zg which is discussed in Section 5.2. The optimal gap spacing is expected to be in the region where the electrode-diaphragm resistance is lower than $R_\mathrm{zg}/2$, and is expected to be highly dependent on the electrode geometry, electrolyser design, and operating conditions.

where V_cell and V_eq are negative for an electrolytic cell. We characterise the ohmic losses in the system with two length scales. Here, $2l_\mathrm{gap}$ gives the length scale of the anodic and cathodic electrode-diaphragm gaps with conductivity κ which depends on the gas fraction inside the gap. The rest of the ohmic losses are represented by an effective length scale l_eff, which would give the same ohmic drop in case the current density j traverses an unobstructed layer of electrolyte with conductivity κ_m. This length scale represents components like the diaphragm which do not depend on gas fraction, and typically $l_\mathrm{eff} \approx 2-4$ mm in a cell with a Zirfon-Perl diaphragm [3,6]. The dependence of the activation overpotential η on current density is neglected. To include the effects of the gas fraction in the electrode-diaphragm gap on the conductivity κ, we take into account the gas distribution in the vertical direction. Conservation of gas gives $\mathrm{d}W_\mathrm{g}/\mathrm{d}z = j\mathcal{V}_\mathrm{m}/nFl_\mathrm{gap}$. Averaging over anode and cathode we may take $1/n \approx \frac{1}{2}(1/2+1/4) = 3/8$. Inserting $W_\mathrm{g} = \frac{W_\mathrm{l}\langle\varepsilon\rangle}{1-\langle\varepsilon\rangle/\varepsilon_\mathrm{m}}$ from Eq. (26) gives

$$\frac{\mathrm{d}}{\mathrm{d}(z/z_\mathrm{c})}\left(\frac{\langle\varepsilon\rangle/\varepsilon_\mathrm{m}}{1-\langle\varepsilon\rangle/\varepsilon_\mathrm{m}}\right) = \frac{j(z)}{j_0} = \frac{1+2l_\mathrm{gap}/l_\mathrm{eff}}{1+2l_\mathrm{gap}\kappa_0/l_\mathrm{eff}\kappa} \tag{31}$$

where $z_\mathrm{c} \equiv \varepsilon_\mathrm{m}\frac{nFl_\mathrm{gap}W_\mathrm{l}}{\mathcal{V}_\mathrm{m}j_0}$ is a characteristic height over which the gas fraction increases, leading to a decrease in current density from its value j_0 at $z = 0$. The second equation in Eq. (31) comes from inserting Eq. (30). Using this and Eq. (18) in Eq. (31) gives a first-order differential equation for $\langle\varepsilon\rangle$ that can be solved numerically. The exact initial slope can be shown to be $j_0' \equiv \frac{\mathrm{d}j}{\mathrm{d}z}|_{z=0} = -\frac{3j_0}{2z_\mathrm{c}}\frac{\varepsilon_\mathrm{m}(2l_\mathrm{gap})}{2l_\mathrm{gap}+l_\mathrm{eff}}$, and in the limit $z \to \infty$ the gas fraction will tend to ε_m, so the conductivity reads $\kappa_\infty = \kappa(\varepsilon_\mathrm{m})$ so the current density tends to $j_\infty = j_0\frac{1+2l_\mathrm{gap}/l_\mathrm{eff}}{1+2l_\mathrm{gap}\kappa_0/l_\mathrm{eff}\kappa_\infty}$.

We find that an excellent analytical approximation to the numerically obtained current density reads

$$j(z) \approx j_\infty + \frac{j_0 - j_\infty}{\left(1 + \frac{2}{2-\varepsilon_m}\frac{z}{z_c'}\right)^{\frac{2-\varepsilon_m}{2}}} \tag{32}$$

where $z_c' = \frac{j_0 - j_\infty}{-j_0'} = \frac{2}{3}\frac{\mathcal{V}_m(j_0 - j_\infty)}{nFl_{gap}W_1}\left(1 + \frac{l_{eff}}{2l_{gap}}\right)$ is a corrected characteristic height. The largest relative error with the numerical solution occurs when $l \gg l_{eff}$ but is less than 5 % for $\varepsilon_m \leq 0.8$. Instead of the Bruggeman's relation (18) we may also use Maxwell's relation $\frac{\kappa}{\kappa_0} = \frac{1-\langle\varepsilon\rangle}{1+\langle\varepsilon\rangle/2}$, which is similarly in agreement with experimental data [17]. Replacing $\kappa_\infty = \kappa_0(1-\varepsilon_m)^{3/2}$ with $\kappa_\infty = \kappa_0\frac{1-\varepsilon_m}{1+\varepsilon_m/2}$, the approximation of Eq. (32) still holds and has even a smaller error compared to the exact numerical result. Very close to $\varepsilon_m \leq 1$ the errors will be larger, but in the limit $\varepsilon_m = 1$ agrees with the exact solution derived in Ref. [17].

5. Results and discussion

5.1. Kinetics

For all experimental configurations the anodic and cathodic electrode potentials have been measured versus their respective Hg/HgO reference electrodes as shown in Fig. 1. The electrode potentials were nearly equal for all experiments in which a spacer was used to create the electrode-diaphragm gap, but were slightly higher for the zero-gap configuration. Therefore, to investigate the reaction kinetics the electrode potentials obtained for all experiments with an electrode-diaphragm spacer were averaged. Fig. 4 shows the averaged anode and cathode potentials. The electrode potentials are modelled with Eq. (33) [56]:

$$E_i = \pm b_i \operatorname{asinh}\left(\frac{j}{2j_{*,i}}\right) + E_{eq,i} \tag{33}$$

with a + for the anode and a - for the cathode. Here E_i is the electrode potential versus RHE converted from the measured potential of the Hg/HgO electrodes using Eq. (1), $b_i = \frac{RT}{\alpha_i F}$ is the Tafel slope, $j_{*,i}$ is the exchange current density, and $E_{eq,i}$ is the equilibrium potential, with subscript a and c denoting anode and cathode, respectively. The overpotential $\eta_i = E_i - E_{eq,i}$ combine to give $\eta = \eta_a - \eta_c$ in the cell voltage expression of Eq. (30).

The Tafel slopes are determined from the experimental data. In the current density range of $j = 100$ to $1000\,A/m^2$ we find a consistent logarithmic dependence of the electrode potential on current density. This range yields an anodic Tafel slope of $2.303b_a = 0.041$ V/dec and a cathodic Tafel slope $2.303b_c = 0.039$ V/dec. These Tafel slopes correspond to charge transfer coefficients of $\alpha_a = 1.72$ and $\alpha_c = 1.76$ for anode and cathode, respectively. The fundamental Butler–Volmer equation for single electron transfer reactions requires the charge transfer coefficient to have a value between 0 and 1. However, for reactions with multiple electron transfer steps, it is possible for the compounded charge transfer coefficient to have a value between 0 and n [57,58]. To determine the other parameters the model in Eq. (33) is then fitted to the experimentally obtained electrode potentials by minimising the sum of squared errors between the model and experimental results in the current density range of $j = 6.67$ to $1431\,A/m^2$. At current densities above $1431\,A/m^2$ an additional linear dependence on current density arises which will be discussed in more detail later in this section. The fitted model results in the exchange current densities $j_{*,a} = 7.1\,A/m^2$ and $j_{*,c} = 31\,A/m^2$ and equilibrium potentials $E_{eq,a} = 1.373$ V and $E_{eq,c} = -0.004$ V versus RHE.

The kinetic parameters obtained from the experiments are used as input parameters in the simulations. A comparison between the experiments, simulations, and electrode potential model from Eq. (33) is shown in Fig. 4. At current densities over $2000\,A/m^2$, the sum of the absolute anodic and cathodic potentials as measured experimentally compared to the reference electrodes is higher than predicted by Eq. (33). The difference between the experimental potential and Eq. (33) follows a linear relationship as shown by the inset plot in Fig. 4, which indicates an ohmic component in the electrode potentials of approximately $3.75\cdot10^{-6}\Omega m^2$ per electrode which, as in Ref. [5] we refer to as transport resistance. For both electrodes combined this gives $R_{tr} = 7.5\cdot10^{-6}\,\Omega m^2$. In this work, the electrode potential is measured relative to a reference electrode placed behind the working electrode. This potential difference typically includes only the reversible potential of the half-reaction and the kinetic overpotential without the added resistance of the diaphragm and electrolyte between the electrodes. Therefore, an additional ohmic potential difference between the reference electrodes and the anode or cathode is not expected based on the setup used in the experiments. A similar ohmic component was also noticed in previous experimental work [5]. Additionally, 2D electrode-resolved simulations by Nishiki et al. [59] show that the current is distributed along the front face, holes, and back side of the electrode. A difference in electrolyte potential can be seen between the bulk electrolyte and the back side of the electrode when the back side of the electrode participates in the reaction. The extent of this potential difference, and thus the transport resistance R_{tr}, depends on the geometry of the electrode, electrolyte conductivity, and kinetic parameters of the electrode.

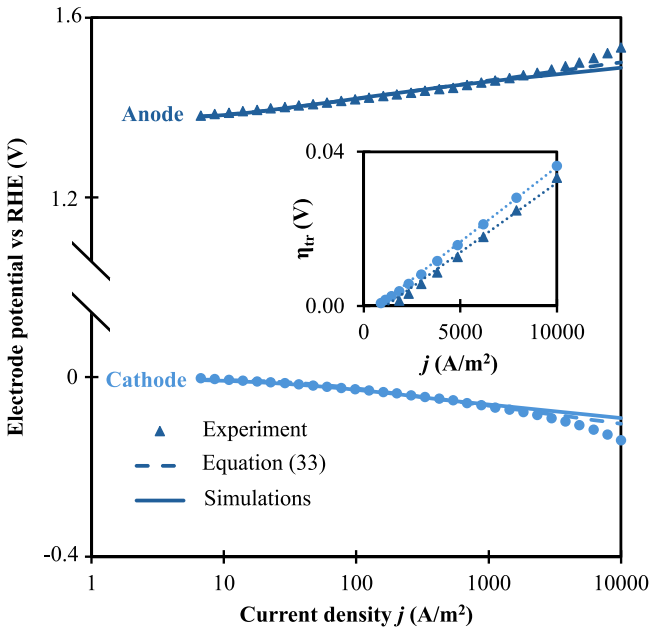

Fig. 4. Electrode potentials versus RHE as a function of current density averaged for all gap width experiments. Symbols represent experimental results, the dashed lines represents the fitted model from Eq. (33) and solid lines represent results from the simulations. The inset plot shows additional transport losses η_{tr}, which represents an additional ohmic component in the measured electrode potential. This is obtained by subtracting Eq. (33) from the electrode potentials measured relative to the reference electrodes. The experiments were carried out at 80 °C in 30 wt.% KOH electrolyte. The same RuO_2 electrodes and Zirfon diaphragm were used in all experiments.

The electrode potentials in the simulations are obtained by taking the difference between the potential of an electrode and the electrolyte potential in the bulk electrolyte. This mimics the two points of measurement in the experiments, with a reference electrode in the bulk electrolyte, which is compared to the electrode potential. The electrode potentials obtained from the simulations are lower than both the experiments and the model Eq. (33). The difference compared to the experiments is expected, as the additional transport resistance R_{tr} is not included in the computational model. The difference with the

model equation requires more explanation. The experimental electrode potentials are measured versus a reference electrode, which is placed behind the electrodes in the bulk electrolyte. Since the electrodes have a finite thickness and have perforations, the current will distribute between the front face, inside the holes, and at the back of the electrodes [59]. This results in a change in electrolyte potential at the back side of the electrodes and in the bulk electrolyte, and a smaller difference between the potential measured by the reference electrode and the anode or cathode. This highlights the shortcomings of using only reference electrodes on the outside of the electrode-diaphragm assembly, in the bulk electrolyte, which fails to capture the effects of current distribution along the electrodes in a typical zero-gap configuration. These effects can be measured by including a third reference electrode, which measures the potential at the diaphragm between the two electrodes, as shown in Ref. [60].

5.2. Gap width

In the experiments, a nylon spacer is introduced in between the electrodes and diaphragm to create a finite electrode-diaphragm gap, shown schematically in Fig. 1. Fig. 5 shows the cell voltage for electrode-diaphragm gap widths of 60 – 910 µm compared to the cell voltage for an otherwise equivalent zero-gap configuration without spacers. The solid lines in Fig. 5 represent the results from the simulations, which compare well with the experimental results for gap widths under 910 µm, excluding the zero-gap. The much narrower spacings between the diaphragm and electrode front that are likely present in a zero-gap configuration will be dominated by surface tension effects, which invalidate key assumptions in the mixture model formulation. Therefore, the zero-gap configuration is not considered in the simulations. The smallest gap of 60 µm exhibited the lowest cell potential for each current density. All larger gaps resulted in a higher cell potential. Since the kinetic overpotentials as measured with reference electrodes are independent of gap width, this increase in cell potential can be explained by an increase in the resistance in between the electrodes. Based on this observation, the zero-gap configuration would be expected to have the lowest cell potential. However, the 60 µm gap also exhibited a lower cell potential than the zero-gap configuration without any spacer.

Repeatability of results with zero-gap configurations is a key challenge in the field of alkaline water electrolysis. The error bars in Fig. 5 represent the average relative error in the cell potential for repeat measurements in between the zero-gap cell has been reconstructed. We find average relative errors of 1%, 1.8%, and 1.3% for current densities of 2330, 6200, and 10^4 A/m^2, respectively. This shows that the cell used in this study gives repeatable results in consecutive experiments. The variation of the measured potentials with time over the measurement window was found to be negligible. However, as exemplified by previous work in literature, reproducibility between different cells can be limited based on operating conditions, cell design, and specifically compression of the electrode-diaphragm assembly [34,61,62].

At a current density of 10^4 A/m^2 the zero-gap configuration has a 34 mV higher cell potential compared to the 60 µm gap and performs similarly to the 210 µm gap. The current distribution is assumed to be optimal for the experiments with a spacer, since the electrode potential measurements show no difference in activation overpotentials for all experiments with electrode-diaphragm spacers. When the electrode is pressed against the diaphragm in a zero-gap configuration, it is hypothesised and shown through imaging that gas accumulated in between the electrode and diaphragm [3,5,6,37]. These bubbles can effectively block some electrode and diaphragm area, leading to increased activation overpotentials at the electrodes and increased ohmic losses over the electrolyte and diaphragm. To investigate this additional overpotential, the potentials for the various gap widths are extrapolated to a gap width of zero. This represents the cell potential of an ideal zero-gap configuration, with minimal resistance and no additional overpotentials.

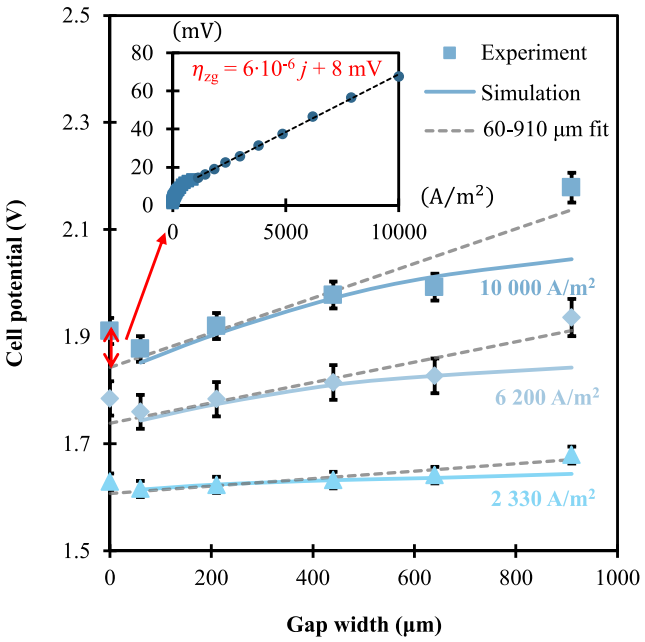

Fig. 5. The measured cell potential at various current densities j for the zero-gap configuration and various widths of the electrode-diaphragm gap. On the x-axis the electrode-diaphragm gap width is shown, which is symmetrically applied to both the anode and cathode. The inset plot shows the zero-gap overpotential η_{zg} on the y-axis as a function of current density on the x-axis. The error bars indicate the average relative error of repeat experiments per current density. The zero-gap overpotential is obtained as the difference between the measured cell potential for the zero-gap configuration and the linear fit of the measured cell potentials for the configurations with l_{gap} = 60–910µm, indicated in the figure by the red arrow on the y-axis. Symbols represent experimental results, and the solid lines represent computational model results. The experiments were carried out at 80 °C in 30 wt% KOH electrolyte. The same RuO_2 electrodes and Zirfon diaphragm were used in all experiments.

The difference between this extrapolated potential and the measured zero-gap potential which we will refer to as the zero-gap overpotential η_{zg}, which is shown in the inset plot of Fig. 5. At lower current densities, η_{zg} mainly consists of kinetic losses, while at higher current densities an additional resistance of approximately $6 \cdot 10^{-6}\,\Omega m^2$ predominates the overpotential. Here, ζ represents the degree of blockage of the electrode and diaphragm surface by bubbles, which can have a value between 0 and 1 where 0 represent no blockage by bubbles and 1 represents full blockage of the electrodes and diaphragm by bubbles. ζ contributes to the zero-gap overpotential by blocking reactive electrode area and by effectively reducing the area available for ionic transport. The relation between ζ and η_{zg} can then be described by

$$\eta_{zg} \approx j R_{eff} \frac{\zeta}{1-\zeta} + b \ln \frac{1}{1-\zeta} \tag{34}$$

where the first term gives the increase in resistance when a fraction ζ of the cross-sectional area available for charge transport is blocked and the second term gives the increase in activation overpotential when a fraction ζ of the electrode surface area is blocked. Here, the effective cell resistance $R_{eff} = R_{dia} + R_{tr}$ is the cell area resistance without zero-gap overpotential or resistance from the electrode-diaphragm gap with $R_{dia} = 1.15 \cdot 10^{-5}\,\Omega m^2$ and $R_{tr} = 0.75 \cdot 10^{-5}\,\Omega m^2$ as discussed in Section 5.1, and b is the combined anodic and cathodic Tafel slope. Here η_{zg} is added to $\eta = \eta_a - \eta_c + \eta_{zg}$ in Eq. (30), only in case of a zero gap. The cell resistance enters as $R_{eff} = l_{eff}/\kappa_0$ into Eq. (30). With the zero-gap overpotential presented in the inset plot of Fig. 5, this gives a blockage of $\zeta \approx 0.25$ for both the ohmic and activation components of the overpotential. While we were not able to directly measure gas

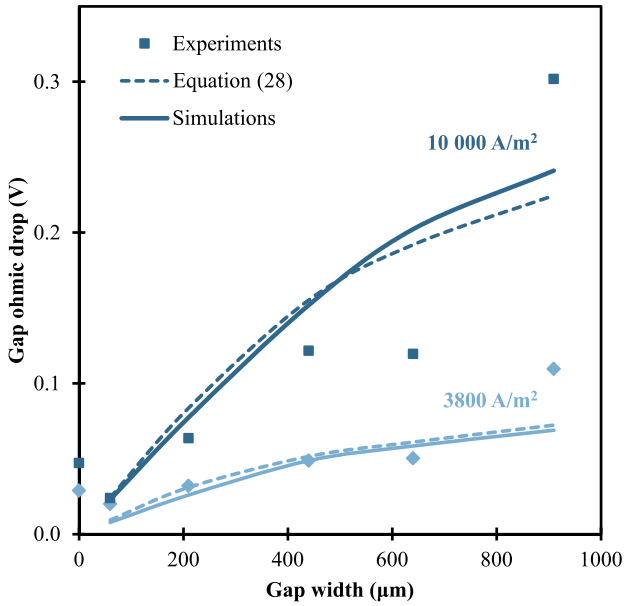

Fig. 6. The ohmic drop over the gap as a function of gap width for current densities of $j = 3800\,\mathrm{A/m^2}$ and $j = 10\,000\,\mathrm{A/m^2}$. The symbols represent estimated gap overpotentials from experimental results, the dashed lines represent gap overpotentials as calculated from Eq. (28) with $\epsilon_m = 0.5$ and $z = 0.04\,\mathrm{m}$, and the solid lines represent gap overpotentials from the simulations. The experimental ohmic drop over the gap is obtained from the difference in potential between the anodic and cathodic reference electrodes. This gives the total electrolyte potential drop over the cell, from which the ohmic drop over the diaphragm jR_{dia} with $R_{dia} = 1.15 \cdot 10^{-5}\,\Omega\mathrm{m}^2$ and the ohmic transport component measured in the electrode potentials jR_{tr} with $R_{tr} = 0.75 \cdot 10^{-5}\,\Omega\mathrm{m}^2$ are subtracted.

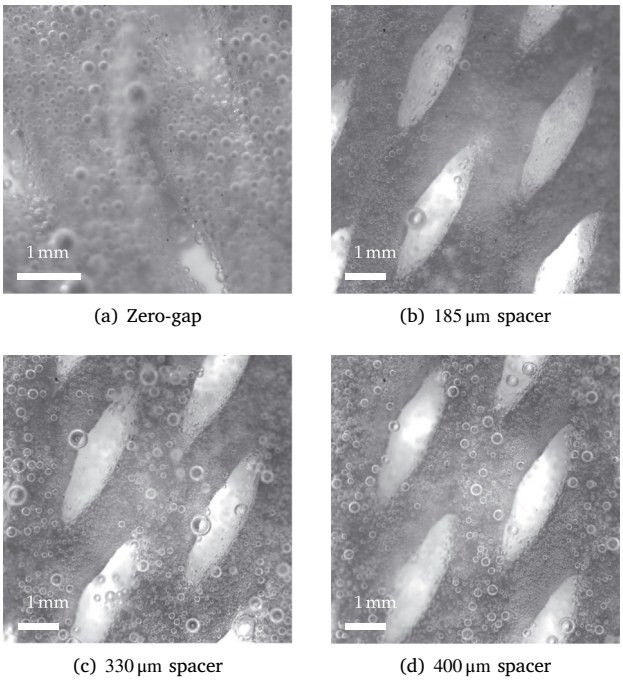

(a) Zero-gap (b) 185 μm spacer

(c) 330 μm spacer (d) 400 μm spacer

Fig. 7. Image stills from videos from the back side, the side facing the bulk electrolyte, of RuO_2 cathodes in (a) a zero-gap configuration and with a (b) 185 μm, (c) 330 μm, and (d) 400 μm spacer. The zero-gap configuration was imaged at a current density of $2600\,\mathrm{A/m^2}$, while the configurations with a spacer in between electrode and diaphragm were imaged at a current density of $1850\,\mathrm{A/m^2}$. The zero-gap configuration was imaged with a different focal length; hence, fewer electrode holes are visible in the frame. These images are reproduced with permission from the work of Craye [37].

fractions in the gap, this seems a plausible value judging from images taken through a transparent membrane (SI Video - Blockage5100Am2). This video was recorded using the set-up described in Ref. [37] and shows gas films in between a membrane and electrode in a zero-gap configuration. Additionally, what gives us some confidence is the internal consistency that a similar fraction is required to explain both the measured activation overpotential and ohmic component of the zero-gap overpotential.

Two reference electrodes measured the drop in electrolyte potential across the electrode-diaphragm assembly in the gap width experiments as shown in Fig. 1. This potential represents the potential difference in the electrolyte across the cell. This total ohmic potential, corrected for the baseline contribution of the diaphragm, is shown in Fig. 6 as a function of the electrode-diaphragm gap width. The simulations and analytical model are in good agreement for the ohmic overpotential due to the gap and capture the trend seen in the experiments. The ohmic overpotential due to the electrode-diaphragm gap increases with increasing gap width, with the lowest potential for a gap width of 60 μm. This indicates that the addition of an electrode-diaphragm gap, as expected, introduces some ohmic losses, and the lower cell potential observed for small gaps is likely due to the mitigation of the zero-gap overpotential.

Fig. 7 shows a side-by-side comparison of pictures of expanded metal electrodes taken from videos in both a zero-gap configuration and with a 185, 330, and 400 μm spacer. The full video files can be found in (SI Videos: Zero-Gap, 185um, 330um, 400um). The videos show that the configurations which include a spacer have visibly fewer and smaller bubbles inside the electrode hole. Additionally, the bubbles visibly flow upwards in between the electrodes and the diaphragm. This shows qualitatively that there is sufficient space between the electrodes and diaphragm to prevent the accumulation of gas bubbles and gas films trapped between the electrodes and diaphragm.

The additional voltage losses in a zero-gap configuration have been reported on in several studies [3,4], and Ref. [6] reported that the addition of a 200 μm electrode-diaphragm gap reduced the cell potential by 0.2 V compared to a zero-gap configuration. The additional losses are attributed to gas film or slug formation in between the electrode and diaphragm, which deactivates part of the electrode. As a result, the current distribution is more inhomogeneous, which increases both the kinetic and ohmic overpotentials around the electrodes. This is consistent with the findings for the zero-gap overpotential in this study. However, in this study, the zero-gap overpotential is lower than found in Ref. [6]. In addition to the zero-gap overpotential, the cell potential shown in Fig. 5 increases significantly with larger electrode-diaphragm gaps due to an increased electrolyte resistance. This ohmic contribution was quantified for the current configuration and operating conditions. In the next section we will discuss the simulation and model-based approach to describing this ohmic potential, which aids in understanding the bubble-induced resistance in the electrode-diaphragm gap.

5.3. Simulation results

It is difficult to accurately determine the gas fraction profile around the electrodes experimentally in alkaline water electrolysis. Therefore, simulations can be a useful tool to give insight into the gas fractions inside the electrode-diaphragm gap. Fig. 8 shows the average gas fraction of the cathode and anode gaps at a current density of $j = 3800\,\mathrm{A/m^2}$ as a function of height and various different gap widths. Over the first few centimetres the simulations predict that the gas fraction increases rapidly with height. At higher gas fractions, however, the rate at which the gas fraction increases is reduced. The analytical model presented in Section 4 reflects this behaviour. When

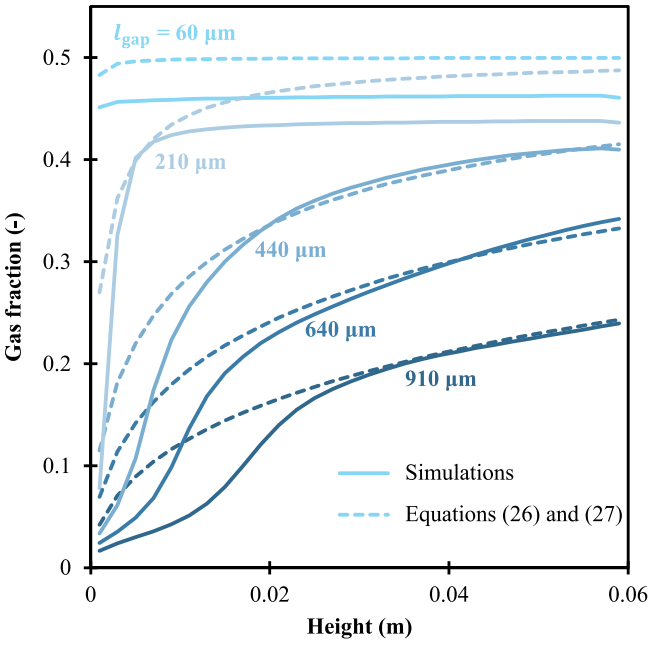

Fig. 8. Gas fractions inside the electrode-diaphragm gap as a function of height for different electrode-diaphragm gap widths and a current density of $j = 3800\,\mathrm{A/m^2}$. The gas fraction represents the average of the cathodic and anodic gap gas fractions.

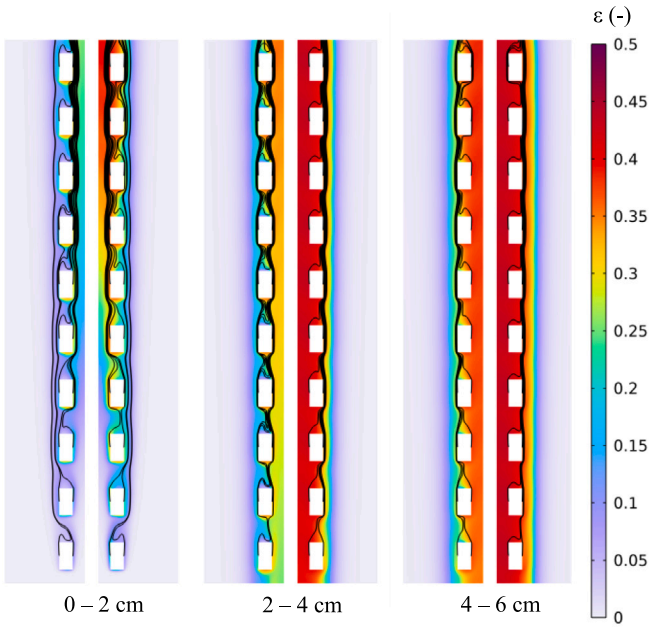

Fig. 9. Two-dimensional gas fraction profile from the simulations using the computational model described in Section 3. The gas fraction profile corresponds to the gap width $l_{gap} = 440\,\mu\mathrm{m}$ shown in Fig. 8, for a current density of $j = 3800\,\mathrm{A/m^2}$. The streamlines represent the volume-averaged mixture velocity **U**. Two streamlines originate from each electrode segment, one on the front side and one on the back side. At the bottom section of the electrodes, the streamlines predominantly move to inside the electrode-diaphragm gap. Once the electrode-diaphragm gap fills with gas the streamlines move towards the back side of the electrodes instead.

gas bubbles are produced at the electrodes, the total gas superficial velocity W_g increases, which leads to a corresponding increase in the gas fraction in the gap ε. The higher gas fraction in the gap increases the buoyancy of the mixture, which results in a higher liquid velocity W_l. However, the inclusion of a maximum gas fraction ε_m also defines a maximum liquid superficial velocity $W_{l,max}$ through equation Eq. (22) and a corresponding maximum gas superficial velocity $W_{g,max}$. The gas superficial velocity increases with current density and height, but also depends on the gap width l_{gap}, as W_g increases more rapidly for smaller gaps. Additionally, smaller gaps will have a lower W_l due to increased viscous friction. This inter-dependence of the liquid and gas superficial velocities and gas fraction results in an asymptotic behaviour where the gas fraction approaches ε_m for high W_g. This asymptotic behaviour occurs more quickly for narrow gaps as well as higher current densities, and can be seen well in Fig. 8.

The bubble movement around the electrodes in the simulations is represented in Fig. 9 by streamlines showing the mixture velocity. The development of the bubble plume around the electrodes can be characterised in two stages. The reaction preferentially takes place on the front of the electrode facing the diaphragm, and initially, the gas fraction mainly increases inside the electrode-diaphragm gap. This results in increased buoyant forces inside the gap, which pull additional liquid and bubbles formed on the outside of the electrode into the gap. This behaviour is also observed in videos of these set-ups (SI Videos: Zero-Gap, 185um, 330um, 400um) and previous studies [63,64]. In the first stage, the gas fraction inside the gap increases while the plume on the back side of the electrode hardly grows, represented by the first two centimetres in Fig. 9. As the gap fills up with gas and the gas fraction approaches 0.5, bubble interactions give rise to the dispersion mechanisms in Eq. (6). While the reaction still mostly occurs inside the gap, bubbles are forced to the outside of the electrode-diaphragm assembly. In the second stage, the bubble plume on the back side of the electrode steadily grows, represented by 2 – 4 cm in Fig. 9.

The gas fraction distribution along the height of the electrolyser additionally results in a non-homogeneous distribution of current along the electrodes. Fig. 10 compares the current distribution along the height of the electrodes for the simulations and the analytical solution given by Eq. (32) for a gap width of 440 µm. The current density from the simulations at $z = 0$ was used as input j_0 for the analytical model. There is good agreement between the simulations and analytical model, with a relative error in the local current density $j(z)$ between 2%–8% for the current densities shown in Fig. 10. At the bottom of the electrodes, the highest local current density is observed. Initially, $j(z)$ decreases rapidly with increasing height, which coincides with the initial increase in the gas fraction around the electrodes. Higher up along the electrodes and for higher current densities, the local current density reaches a steady value j_∞ when the gas fraction approaches $\varepsilon_m = 0.5$. This is reached more quickly for higher average current densities and lower gap widths.

Under the atmospheric pressures used in this work and gap widths under 500 µm, $j(z)$ shows a large drop over the first few centimetres and typically stabilises at heights under 10 cm. However, at the elevated pressures used in industry the volume of the produced gas is significantly lower, and the height over which the current stabilises will be considerably higher. For instance, at a geometrical current density of $j = 10^4\,\mathrm{A/m^2}$ and gap width $l_{gap} = 440\,\mu\mathrm{m}$, a pressure of 1 bar gives a critical height of $z_c' \approx 7\,\mathrm{cm}$, while at 30 bar this gives a critical height of $z_c' \approx 65\,\mathrm{cm}$. The model presented here can be used to give an initial prediction of the current distribution in an electrolysis cell with a near-zero-gap electrode configuration.

5.4. Optimal electrode-diaphragm gap width

The analytical model predicts the existence of an optimal gap width for high maximum gas fractions. However, there only exists an absolute minimum in the gap resistance for the case where the maximum gas fraction $\varepsilon_m = 1$. A local minimum in the gap resistance exists for $\varepsilon_m > 0.7$. For maximum gas fractions lower than this, this model

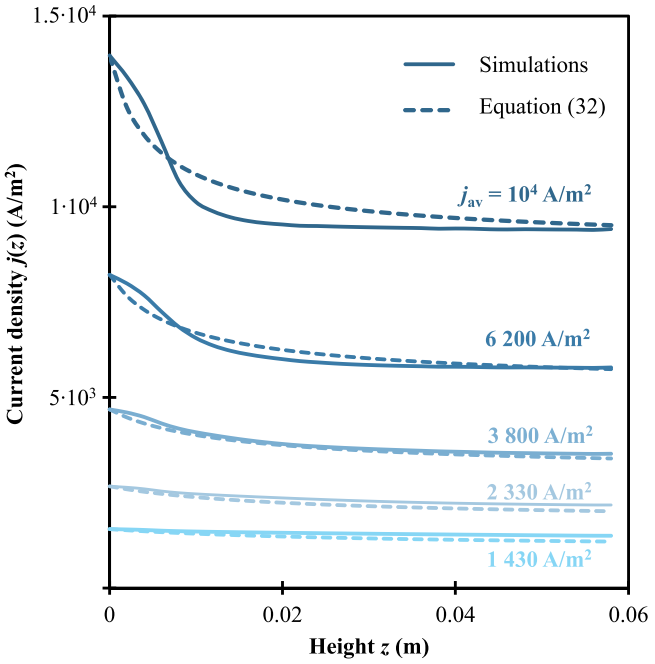

Fig. 10. Distribution of the local current density $j(z)$ with height in the electrolyser z for an electrode-diaphragm gap width of l_{gap} = 440 µm and for average geometrical current densities of 1430 A/m^2, 2330 A/m^2, 3800 A/m^2, 6200 A/m^2, and 10^4 A/m^2. The solid lines represent the current distribution obtained from the simulations, averaged per electrode segment pair, and the dashed lines represent the analytical model solution Eq. (32).

predicts no optimal gap width and predicts a minimal resistance for a gap width of 0 µm. As shown in Fig. 6, the gap overpotential in the simulations, experiments, and analytical model shows good agreement with a highest observed gas fraction of approximately 0.5 in the simulations and ε_m = 0.5 for the analytical model. However, the experiments also show that the inclusion of a small gap results in a lower cell potential than zero-gap by avoiding the additional zero-gap induced losses η_{zg}. The zero-gap overpotential is likely due to local blocking of the diaphragm and electrode surface area, which results in an inhomogeneous distribution of the current. This increases the activation overpotential and increases the effective diaphragm resistance [39]. Several works previously found that the inclusion of a small electrode-diaphragm gap improves the cell potential [4,6,33]. However, for instance the work in Ref. [34] finds that a zero-gap outperforms configurations with electrode-diaphragm spacings between 0.1–0.3 mm and gives as possible explanation the reduced compression of the electrode-diaphragm assembly in their cell design. The work in Ref. [61] found an optimum in cell potential for the mechanical compression of a zero-gap electrolyser. From this, it can be inferred that a higher degree of compression likely leads to a higher zero-gap overpotential. Additionally, lower compression can allow a small gap to exist. Analysis of the zero-gap overpotential in this study indicates a blockage of roughly 25%, based on the model in Eq. (34). The expected optimal gap width is then large enough to avoid the zero-gap induced overpotential, but small enough to prevent a significant ohmic contribution, in the order of 100 µm. A gap width of this size represents an engineering challenge to include in large industrial-scale electrolysers, but could for instance be achieved with structured protrusions or spacer wires on the diaphragm [65,66]. The impact of the zero-gap losses likely depends on the design of the electrodes, as geometrical characteristics like the hole size can significantly influence the cell potential in a zero-gap configuration [5]. The optimal gap width, therefore, depends on the design of the electrolyser and the electrodes and the effect of the electrode geometry on gas transport around the electrodes.

6. Conclusions

We experimentally investigated the influence of electrode-diaphragm gap width on the performance of a lab-scale alkaline water electrolysis cell. An electrode-diaphragm gap width of 60 µm resulted in the lowest cell potential and ohmic losses, outperforming the gap widths of 210–910 µm and the traditional zero-gap configuration with no electrode-diaphragm gap.

The measured electrode potentials show the expected kinetic overpotentials as well an additional ohmic component. A similar ohmic component was already described in a previous theoretical work in literature [59]. Recent experimental work again found a similar component in the electrode potential, and the extent of this additional ohmic component increases with decreasing electrode hole size [5]. Similarly, the zero-gap overpotential is expected to depend on the electrode shape, and a good understanding of the interaction between the ohmic and kinetic losses in the electrodes in a zero-gap configuration is important in order to further optimise electrolysers for alkaline water electrolysis.

We extended an analytical model for electrodes with perforations, which predicts the gas fraction and fluid flow velocities inside the electrode-diaphragm gap. This model can approximate the ohmic resistance of the electrode-diaphragm gap and vertical current distribution of the near-zero gap configuration. The analytical model predicts, in agreement with the simulations, that the current distribution decreases primarily over the first few centimetre of the electrodes. For maximum gas fractions higher than 0.7, a local optimum exists for the ohmic resistance of the gap, while for maximum gas fractions under 0.7 the ohmic resistance always increases with increasing gap width.

The zero-gap configuration incurs an additional zero-gap overpotential. This overpotential is most likely due to the accumulation of gas bubbles and films in between the electrode and the diaphragm. The inclusion of a small electrode-diaphragm gap mitigates this zero-gap overpotential and reduces the cell potential. This gap, however, does add an ohmic penalty, and as such the optimal electrode-diaphragm gap width should be large enough to mitigate the zero-gap overpotential but small enough to minimise additional ohmic losses. As the severity of zero-gap overpotential depends on the characteristics of the electrodes and design of the electrolyser, the optimal gap width depends on the design of the electrodes used.

CRediT authorship contribution statement

W.L. van der Does: Writing – review & editing, Writing – original draft, Visualization, Validation, Project administration, Methodology, Formal analysis, Data curation, Conceptualization. **N. Valle:** Writing – review & editing, Supervision, Methodology. **J.W. Haverkort:** Writing – review & editing, Writing – original draft, Supervision, Methodology, Funding acquisition, Conceptualization.

Declaration of competing interest

The authors declare that they have no known competing financial interests or personal relationships that could have appeared to influence the work reported in this paper.

Acknowledgments

We thank E.J.B. Craye for the insightful images and videos shown in this article.

Appendix A. Supplementary data

Supplementary material related to this article can be found online at https://doi.org/10.1016/j.electacta.2026.148509.

Data availability

Data will be made available on request.

References

[1] T. Smolinka, H. Bergmann, J. Garche, M. Kusnezoff, The history of water electrolysis from its beginnings to the present, in: Electrochemical Power Sources: Fundamentals, Systems, and Applications, Elsevier, 2022, pp. 83–164.

[2] R. Phillips, A. Edwards, B. Rome, D.R. Jones, C.W. Dunnill, Minimising the ohmic resistance of an alkaline electrolysis cell through effective cell design, Int. J. Hydrog. Energy 42 (38) (2017) 23986–23994.

[3] M.T. de Groot, A.W. Vreman, Ohmic resistance in zero gap alkaline electrolysis with a Zirfon diaphragm, Electrochim. Acta 369 (2021).

[4] V. Kienzlen, D. Haaf, W. Schnurnberger, Location of hydrogen gas evolution on perforated plate electrodes in zero gap cells, Int. J. Hydrog. Energy 19 (1994) 729–732.

[5] J.W. Haverkort, A.S. Aghdam, E.J.B. Craye, The optimal electrode hole size in zero gap alkaline water electrolysis: A combined electrochemical, theoretical, and bubble imaging approach, Int. J. Hydrog. Energy 171 (2025) 150919.

[6] J.W. Haverkort, H. Rajaei, Voltage losses in zero-gap alkaline water electrolysis, J. Power Sources 497 (2021).

[7] V. Schröder, K. Holtappels, Explosion Characteristics of Hydrogen-Air and Hydrogen-Oxygen Mixtures at Elevated Pressures, Hydrogen Knowledge Centre, 2005.

[8] R.L.G. Barros, J.T. Kraakman, C. Sebregts, J. van der Schaaf, M.T. de Groot, Impact of an electrode-diaphragm gap on diffusive hydrogen crossover in alkaline water electrolysis, Int. J. Hydrog. Energy 49 (2024) 886–896.

[9] C.W. Tobias, Effect of gas evolution on current distribution and ohmic resistance in electrolyzers, J. Electrochem. Soc. 106 (9) (1959) 833.

[10] N. Nagai, M. Takeuchi, T. Kimura, T. Oka, Existence of optimum space between electrodes on hydrogen production by water electrolysis, Int. J. Hydrog. Energy 28 (1) (2003) 35–41.

[11] F. Hine, M. Yasuda, R. Nakamura, T. Noda, Hydrodynamic studies of bubble effects on the IR-drops in a vertical rectangular cell, J. Electrochem. Soc. 122 (9) (1975) 1185.

[12] G. Kreysa, M. Kuhn, Modelling of gas evolving electrolysis cells. I. The gas voidage problem, J. Appl. Electr. 15 (4) (1985) 517–526.

[13] H. Kellermann, K. Ju¨ ttner, G. Kreysa, Dynamic modelling of gas hold-up in different electrolyte systems, J. Appl. Electr. 28 (3) (1998) 311–319.

[14] E.L.J. Coenen, L.J.J. Janssen, Voidage of bulk solution in a tall vertical gasevolving cell, J. Appl. Electr. 27 (1997) 1143–1148.

[15] H. Zhang, R. Zhang, Z. Chen, F. Yuan, Q. Yang, B. Liu, Experimental and theoretical study on the gas holdup feature in a 1.5-m tall alkaline water electrolytic cell, AIChE J. 71 (6) (2025) e18814.

[16] H. Vogt, The voidage problem in gas-electrolyte dispersions, J. Appl. Electr. 17 (2) (1987) 419–426.

[17] J.W. Haverkort, Electrolysers, Fuel Cells and Batteries: Analytical Modelling, TU Delft Open Publishing, 2024.

[18] G.B. Deiters, J.R. de Vries, J.W. Haverkort, An experimentally validated analytical model for natural electrolyte recirculation in an alkaline water electrolyser, Int. J. Hydrog. Energy 188 (2025) 152053.

[19] W. Thiele, M. Schleiff, Zur Optimierung der Geometrischen Abmessungen Vertikaler Elektrolyseure mit Gasentwickelnden Elektroden, 1979.

[20] F. Hine, K. Murakami, Bubble effects on the terminal voltage of a vertical cell with perforated electrodes, J. Electrochem. Soc. 128 (1981) 64.

[21] J. Jorne, J.F. Louvar, Gas-diverting electrodes in the chlor-alkali membrane cell, J. Electrochem. Soc. 127 (2) (1980) 298.

[22] L.J.J. Janssen, J.J.M. Geraets, E. Barendrecht, S.D.J. Van Stralen, Ohmic potential drop during alkaline water electrolysis, Electrochim. Acta 27 (9) (1982) 1207–1218.

[23] H. Vogt, A hydrodynamic model for the ohmic interelectrode resistance of cells with vertical gas evolving electrodes, Electrochim. Acta 26 (9) (1981) 1311–1317.

[24] N. Nagai, M. Takeuchi, M. Nakao, Effects of generated bubbles between electrodes on efficiency of alkaline water electrolysis, JSME Int. J. Ser. B Fluids Therm. Eng. 46 (4) (2003) 549–556.

[25] L.R. Czarnetzki, L.J.J. Janssen, Electrode current distribution in a hypochlorite cell, J. Appl. Electr. 19 (5) (1989) 630–636.

[26] J.M. Bisang, Current distribution in a gas-evolving electrochemical reactor with an expanded metal electrode, J. Appl. Electr. 22 (6) (1992) 585–587.

[27] J.M. Bisang, Theoretical and experimental studies of current distribution in gas-evolving electrochemical reactors with parallel-plate electrodes, J. Appl. Electr. 21 (9) (1991) 760–766.

[28] J.M. Bisang, Effect of mass transfer on the current distribution in monopolar and bipolar electrochemical reactors with a gas-evolving electrode, J. Appl. Electr. 23 (10) (1993) 966–974.

[29] Y. Nishiki, K. Aoki, K. Tokuda, H. matsuda, Effect of gas evolution on current distribution and ohmic resistance in a vertical cell under forced convection conditions, J. Appl. Electr. 16 (4) (1986) 615–625.

[30] A. Martin, A. Wragg, The vertical distribution of current in a gas-evolving membrane cell, J. Appl. Electr. 19 (5) (1989) 657–667.

[31] Z. Nagy, Calculations on the effect of gas evolution on the current-overpotential relation and current distribution in electrolytic cells, J. Appl. Electr. 6 (2) (1976) 171–181.

[32] I. Roušar, V. Cezner, J. Nejepsova, M. Jackšić, M. Spasojević, B. Nikolić, Calculation of local current densities and terminal voltage for a monopolar sandwich electrolyser: application to chlorate cells, J. Appl. Electr. 7 (5) (1977) 427–435.

[33] J. Divišek, P. Malinowski, Electrolyzer with sandwich arrangement of diaphragm and electrodes and method of producing the sandwich arrangement, 1988, Google Patents, US Patent 4, 773, 982.

[34] O.-Y. Dung, S. Boden, A.W. Vreman, N.G. Deen, M. Schubert, Y. Tang, X-ray measurements of gas distribution in a zero gap alkaline water electrolyzer, Int. J. Hydrog. Energy 105 (2025) 835–844.

[35] M.R. Kraglund, Alkaline membrane water electrolysis with non-noble catalysts, 2017, Department of Energy Conversion and Storage, Technical University of Denmark.

[36] H. Qiu, K. Obata, K. Tsuburaya, T. Nishimoto, K. Nagato, K. Takanabe, Impact of gas bubble slug on high-frequency resistance and cell voltage in water electrolysis device, J. Power Sources 611 (2024) 234765.

[37] E. Craye, Bubble quantification: in the near electrode region in alkaline water electrolysis, 2023.

[38] Y. Nishiki, Current distribution in a two-dimensional narrow gap cell composed of a gas evolving electrode with an open part, J. Appl. Electr. 17 (1987) 67–76.

[39] W.L. van der Does, N. Valle, J.W. Haverkort, Multiphase alkaline water electrolysis simulations: The need for a solid pressure model to explain experimental bubble overpotentials, Int. J. Hydrog. Energy 102 (2025) 295–303.

[40] K. Kawashima, R.A. Márquez, Y.J. Son, C. Guo, R.R. Vaidyula, L.A. Smith, C.E. Chukwuneke, C.B. Mullins, Accurate potentials of Hg/HgO electrodes: practical parameters for reporting alkaline water electrolysis overpotentials, Acs Catal. 13 (3) (2023) 1893–1898.

[41] J.N. Hausmann, B. Traynor, R.J. Myers, M. Driess, P.W. Menezes, The pH of aqueous NaOH/KOH solutions: a critical and non-trivial parameter for electrocatalysis, ACS Energy Lett. 6 (10) (2021) 3567–3571.

[42] G. Salvi, A. DeBethune, The temperature coefficients of electrode potentials: II. The second isothermal temperature coefficient, J. Electrochem. Soc. 108 (7) (1961) 672.

[43] J.W. Haverkort, An analytical model for shunt currents in electrolyser, fuel cell, and flow battery stacks, J. Power Sources 670 (2026) 239447.

[44] M. Ishii, T. Hibiki, Thermo-Fluid Dynamics of Two-Phase Flow, Springer Science & Business Media, 2011.

[45] A.A. Dahlkild, Modelling the two-phase flow and current distribution along a vertical gas-evolving electrode, J. Fluid Mech. 428 (2001) 249–272.

[46] G. Kreysa, M. Kuhn, Modelling of gas evolving electrolysis cells. I. The gas voidage problem, J. Appl. Electr. 15 (4) (1985) 517–526.

[47] T.T. Duignan, The surface potential explains ion specific bubble coalescence inhibition, J. Colloid Interface Sci. 600 (2021) 338–343.

[48] M. Ishii, N. Zuber, Drag coefficient and relative velocity in bubbly, droplet or particulate flows, AIChE J. 25 (5) (1979) 843–855.

[49] COMSOL, CFD Module User's Guide, 2023, COMSOL, URL: https://doc.comsol.com/6.2/doc/com.comsol.help.cfd/CFDModuleUsersGuide.pdf.

[50] P.C. Johnson, P. Nott, R. Jackson, Frictional–collisional equations of motion for participate flows and their application to chutes, J. Fluid Mech. 210 (1990) 501–535.

[51] B. Brangeon, P. Joubert, A. Bastide, Influence of the dynamic boundary conditions on natural convection in an asymmetrically heated channel, Int. J. Therm. Sci. 95 (2015) 64–72.

[52] H. Sun, R. Li, E. Chénier, G. Lauriat, On the modeling of aiding mixed convection in vertical channels, Heat Mass Transf. 48 (7) (2012) 1125–1134.

[53] G. Desrayaud, E. Chénier, A. Joulin, A. Bastide, B. Brangeon, J. Caltagirone, Y. Cherif, R. Eymard, C. Garnier, S. Giroux-Julien, et al., Benchmark solutions for natural convection flows in vertical channels submitted to different open boundary conditions, Int. J. Therm. Sci. 72 (2013) 18–33.

[54] J. Rodríguez, S. Palmas, M. Sánchez-Molina, E. Amores, L. Mais, R. Campana, Simple and precise approach for determination of Ohmic contribution of diaphragms in alkaline water electrolysis, Membranes 9 (10) (2019) 129.

[55] P. Habibi, A. Rahbari, S. Blazquez, C. Vega, P. Dey, T.J.H. Vlugt, O.A. Moultos, A new force field for OH–for computing thermodynamic and transport properties of H2 and O2 in aqueous NaOH and KOH solutions, J. Phys. Chem. B 126 (45) (2022) 9376–9387.

[56] F. Hine, Electrode Processes and Electrochemical Engineering, Springer Science & Business Media, 2012.

[57] R. Parsons, General equations for the kinetics of electrode processes, Trans. Faraday Soc. 47 (1951) 1332–1344.

[58] G. Fraser, R. Barradas, A simplified calculation of tafel slopes for successive electrochemical reactions, J. Electrochem. Soc. 112 (4) (1965) 462.

[59] Y. Nishiki, K. Aoki, K. Tokuda, H. Matsuda, Secondary current distribution in a two-dimensional model cell composed of an electrode with an open part, J. Appl. Electr. 16 (2) (1986) 291–303.
[60] P. Leuaa, M.R. Kraglund, C. Chatzichristodoulou, Decoupling of reaction overpotentials and ionic transport losses within 3D porous electrodes in zero-gap alkaline electrolysis cells, Electrochim. Acta 470 (2023) 143306.
[61] R. Phillips, C.W. Dunnill, Zero gap alkaline electrolysis cell design for renewable energy storage as hydrogen gas, RSC Adv. 6 (102) (2016) 100643–100651.
[62] S. Appelhaus, L. Ritz, S.-V. Pape, F. Lohmann-Richters, M.R. Kraglund, J.O. Jensen, F. Massari, M. Boroomandnia, M. Romanò, J. Albers, et al., Benchmarking performance: a round-robin testing for liquid alkaline electrolysis, Int. J. Hydrog. Energy 95 (2024) 1004–1010.
[63] C. Elsner, F. Coeuret, Potential distribution along gas evolving electrodes, J. Appl. Electr. 15 (1985) 567–574.
[64] M. Kuhn, G. Kreysa, Modelling of gas-evolving electrolysis cells. II. Investigation of the flow field around gas-evolving electrodes, J. Appl. Electr. 19 (5) (1989) 677–682.
[65] J. Divišek, et al., Diaphragm for alkaline electrolysis and method for producing the same, 1986, DE3424203A1, URL: https://patents.google.com/patent/DE3424203A1/en.
[66] J. Divišek, Apparatus and method for electrode gap spacing control, 1992, CA1327773C, URL: https://patents.google.com/patent/CA1327773C/en.